

LSP-DETR: Efficient and Scalable Nuclei Segmentation in Whole Slide Images

Matěj Pekár^a, Vít Musil^{a,*}, Rudolf Nenutil^c, Petr Holub^b, Tomáš Brázdil^a

^a*Masaryk University, Faculty of Informatics,
Botanická 68a, Brno, 602 00, Czech Republic*

^b*Masaryk University, Institute for Computer Science,
Šumavská 525/33, Brno, 602 00, Czech Republic*

^c*Masaryk Memorial Cancer Institute,
Žlutý kopec 7, Brno, 656 53, Czech Republic*

Abstract

Precise and scalable instance segmentation of cell nuclei is essential for computational pathology, yet gigapixel Whole-Slide Images pose major computational challenges. Existing approaches rely on patch-based processing and costly post-processing for instance separation, sacrificing context and efficiency. We introduce LSP-DETR (Local Star Polygon DEtection TRansformer), a fully end-to-end framework that uses a lightweight transformer with linear complexity to process substantially larger images without additional computational cost. Nuclei are represented as star-convex polygons, and a novel radial distance loss function allows the segmentation of overlapping nuclei to emerge naturally, without requiring explicit overlap annotations or handcrafted post-processing. Evaluations on PanNuke and MoNuSeg show strong generalization across tissues and state-of-the-art efficiency, with LSP-DETR being over five times faster than the next-fastest leading method. Code and models are available at <https://github.com/RationAI/lsp-detr>.

Keywords: Nuclei Instance Segmentation, Computational Pathology, Transformer Architecture, Star-convex Polygons

^{*}Corresponding author

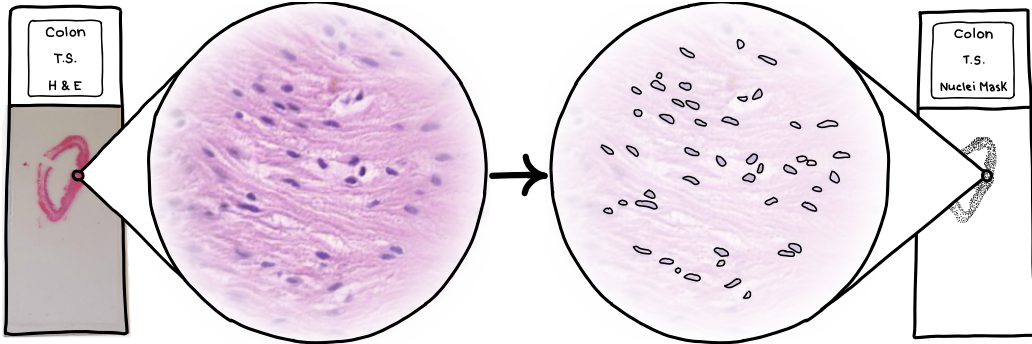


Figure 1: Nuclei instance segmentation on a whole-slide image. The goal is to segment all individual cell nuclei. The algorithm must be scalable and robust to various tissue types.

1. Introduction

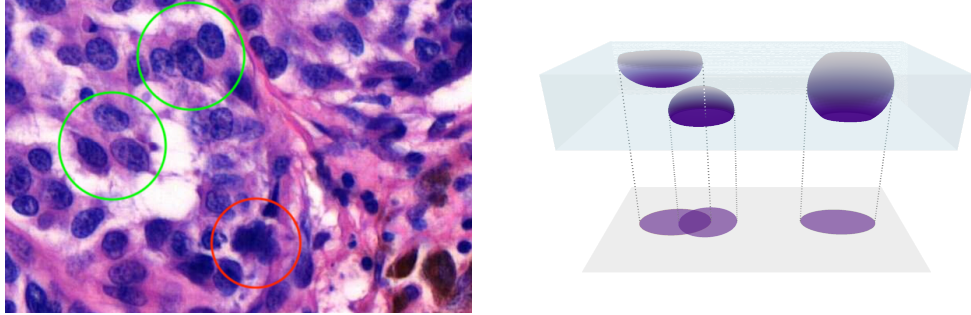
The visualisation of cell nuclei is a prerequisite for histological analysis of tissue, including disease diagnosis, with a particular emphasis on cancer. For decades, nuclear morphology, encompassing variations in size, shape, and texture, has been one of the primary criteria for cancer detection, grading, and prognosis. The spatial arrangement of nuclei also provides crucial information regarding tissue types.

In the field of digital pathology, significant advancements have been made in nuclei segmentation algorithms [1], leading to their integration into widely-used software platforms such as QuPath and HALO. These algorithms are an essential prerequisite for more sophisticated artificial intelligence applications, including graph neural networks, which analyze the intricate relationships and spatial organization of nuclei (see [2] for a comprehensive overview).

1.1. Problem Formulation

We focus on designing a *fast and scalable* algorithm for the problem of *cell nuclei instance segmentation in whole-slide images (WSI) of hematoxylin-eosin-stained tissue samples*, including *overlapping nuclei* in two-dimensional WSIs due to their configuration in the three-dimensional physical tissue (see Figure 2b).

Our goal is to develop a universally applicable system across a wide range of WSIs from different tissues, organs, and pathological alterations. We concentrate on hematoxylin-eosin-stained WSI, but our method can also be applied to different stainings, assuming detailed nuclei annotations. Solving



(a) An example of an H&E-stained image. The green areas highlight delineated or overlapping nuclei. In the red area, an accurate nuclei segmentation is impossible.

(b) Illustration of how nuclei overlap occurs as a result of the tissue slicing and the scanning process.

Figure 2: Ambiguous boundaries and overlaps pose one of the challenges in nuclei segmentation.

the cell nuclei instance segmentation problem in WSI poses several key challenges:

Large data variability. Whole-slide images can vary significantly across multiple dimensions. First, tissue morphology differs substantially across organs, pathological alterations, and even within a single WSI. Nuclei exhibit wide variability in shape, size, and density, and their boundaries are often ambiguous due to overlapping structures and staining limitations, as illustrated in Fig. 2. To develop a generic and universally applicable segmentation algorithm, one must also account for variations in tissue preparation, staining protocols, and pathology practices that differ across laboratories.

Large image size. WSIs are typically gigapixel-scale images, making full-resolution processing computationally infeasible. Common solutions include either downsampling or tiling, i.e., cutting the large image into smaller rectangular patches/tiles. While downsampling is computationally efficient, it often sacrifices the fine detail necessary for accurate nuclei segmentation. Tiling is more widely used but presents its own challenges, particularly with nuclei located at tile boundaries. Overlapping tiles can alleviate this issue, but at the cost of significantly increased computational requirements, especially when using smaller tile sizes.

These characteristics of the nuclei segmentation problem pose difficulties across all phases of the development pipeline, from the acquisition of

large-scale WSI, through the robustness and generalizability of segmentation algorithms, to evaluation, where generating high-quality annotations of individual cell nuclei is both labor-intensive and time-consuming.

1.2. State of the Art

The cell nuclei segmentation problem has been extensively studied in various contexts [3, 4, 5]. Classical approaches, typically based on watershed methods, are still employed in small-scale applications, such as segmenting nuclei instances in a single slide [6]. These methods are simple, interpretable, and computationally efficient. However, they struggle to cope with the data variability encountered in large-scale applications involving numerous images from diverse sources.

More robust machine learning-based methods have been proposed in many studies, see, e.g., [3, 7, 8]. These are often tailored to address specific downstream tasks, for example, prostate cancer grading through nuclei cluster analysis [7], or nuclei classification using transformer-based models [8]. Nonetheless, several works have aimed at developing more universal solutions for nuclei segmentation across diverse WSI datasets [9].

To the best of our knowledge, the existing segmentation methods face critical limitations. Some are tied to specific image sizes [10, 11, 12, 13], leading to inefficiencies in training or inference, as the annotated data usually consists of small tiles. Others rely on computationally expensive hand-crafted post-processing pipelines [14, 15, 4, 16, 17], which hinder the accurate segmentation of overlapping nuclei and add unnecessary complexity.

1.3. Contribution: LSP-DETR

Our solution to the nuclei segmentation problem is a deep-learning algorithm that identifies individual cell nuclei in a given WSI and accurately delineates their boundaries, as shown in Figure 1. The core of the algorithm, addressing challenges mentioned in Section 1.1, is the Local Star Polygon DEtection TRansformer (LSP-DETR), the first fully end-to-end nuclei instance segmentation algorithm. The model takes a microscopy image as input and predicts a set of nuclei, each represented by a star-convex polygon.

The architecture is based on the state-of-the-art object detection framework DETR [18] utilizing transformers. The whole model is accelerated on a GPU, avoiding any CPU-bound pre- or post-processing phases. This end-to-end approach allows for more accurate segmentations, including overlapping nuclei, and simultaneously reduces its computational and memory overhead.

Table 1: Comparison of nuclei segmentation methods. Summarized key characteristics such as post-processing requirements, overlap-prediction capabilities, adaptability to arbitrary input sizes during inference, and inference speed.

Method	End-to-end	Overlaps	Any Image Size	Inference time
StarDist [16]	–	✓*	✓	2.85 s/mm ²
CPP-Net [14]	–	✓*	✓	21.21 s/mm ²
HoVer-NeXt [19]	–	–	✓	2.38 s/mm ²
LKCell [15]	–	–	✓	4.39 s/mm ²
CellViT [11]	–	–	–	13.24 s/mm ²
LSP-DETR	✓	✓	✓	0.46 s/mm ²

* The method was penalized for segmenting overlaps during training.

In summary, LSP-DETR brings the following improvements upon the existing methods:

1. Provides an end-to-end cell nuclei instance segmentation without any pre- or post-processing.
2. Resolves nuclei overlaps robustly. It estimates the shape of the overlapped nucleus even though it is not visible in the image.
3. It is fast and scalable. Our method is multiple times faster and memory-efficient than state-of-the-art methods.

A basic comparison to the existing methods is summarized in Table 1.

Let us briefly overview how the model operates. Each nucleus is represented by its *shape descriptor* consisting of a position vector $p \in \mathbb{R}_+^2$ (image coordinates) and a sequence $r \in \mathbb{R}_+^{64}$, representing radial distances from p along 64 evenly distributed rays, see Figure 3a. These polygons can approximate any star-convex region.

Initially, we cover the input image with descriptors approximating circles and distribute them evenly in a regular grid. The core idea behind LSP-DETR is to iteratively adjust the descriptors so that each is segmenting a nucleus within its neighbourhood, see Figure 3b.

Working directly with shape descriptor instances eliminates any need for post-processing, significantly reducing the computational overhead. Our framework represents a significant step forward in making nuclei segmentation scalable, efficient, and accessible for diverse clinical and research applications.

The technical contribution of this paper is as follows:

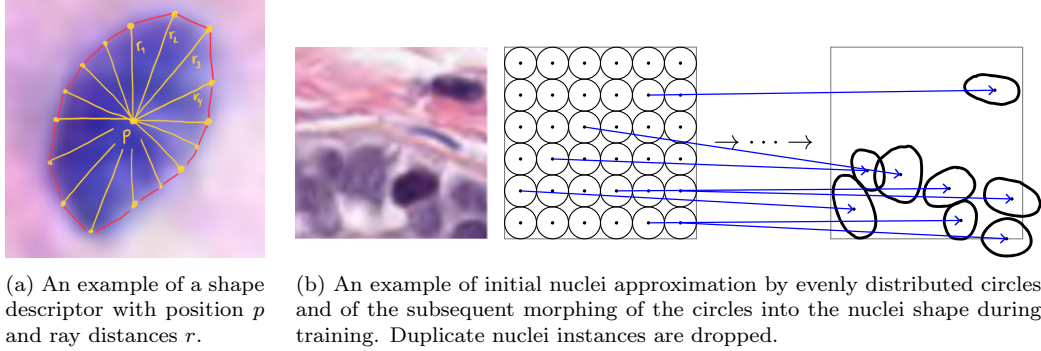


Figure 3: Illustration of the LSP-DETR training process.

1. LSP-DETR relies solely on relative positional information and local context. Predicting star-convex polygons offers a flexible and accurate alternative to traditional bounding boxes.
2. Our LSP-DETR method has been evaluated on the challenging Pan-Nuke benchmark [20], demonstrating a significant improvement in efficiency over well-known methods such as StarDist [16].

2. Related Work

Various methods have been developed for nuclei instance segmentation, ranging from classical image processing approaches to advanced automated deep learning techniques. Despite advancements, there is no canonical deep learning model capable of directly performing set prediction for instance segmentation. Current approaches rely on indirect strategies such as two-stage detectors, one-stage detectors with post-processing, or DETR-like methods.

2.1. Two-Stage Detectors

Two-stage methods typically begin by generating region proposals via bounding box prediction, followed by a segmentation stage that produces the final masks. Mask-RCNN [21] is the most prominent example of this category. Vuola et al. [22] combined Mask-RCNN with U-Net [23], leveraging the strengths of both architectures to improve nuclei segmentation accuracy. Similarly, Bancher et al. [24] augmented Mask-RCNN by including distance maps predicted by U-Net as additional inputs, enabling more precise nuclei separation.

Other works have extended the two-stage framework with additional stages to refine segmentation. For instance, Song et al. [25] proposed a three-stage approach consisting of segmentation, cell labeling, and cell boundary refinement. Although effective, this method is very slow and not designed for end-to-end training, making it less practical for large-scale applications.

While effective, these methods are computationally complex and often require additional post-processing steps to handle overlapping nuclei and deduplication.

2.2. One-Stage Detectors with Post-processing

One-stage detectors simplify the segmentation process by using a single network for prediction, with post-processing techniques to resolve overlapping nuclei and ensure instance separation. DIST [26], for instance, employs a U-Net-style Fully Convolutional Network (FCN) to predict a distance map where each pixel’s value represents its distance to the nearest background pixel. The resulting distance map is post-processed using a watershed algorithm. HoVer-Net [4] introduced a multi-branch decoder network that predicts horizontal and vertical distance maps alongside a binary mask and class mask. These outputs are processed using the watershed algorithm to create nuclei instances. Building on this, CellViT [11] improved HoVer-Net by unifying the decoder branches and incorporating the Segment Anything Model (SAM) [27] for enhanced feature extraction. Further advancements were made by LKCell [15], which replaced computationally expensive SAM with large convolutional kernels [28], achieving superior accuracy. Most recently, CellViT⁺⁺ [29] attempted to replace the SAM feature extractor with pathological foundation models, though this approach failed to yield the expected performance gains.

Another category of one-stage detectors focuses on predicting shape descriptors for each nucleus, describing them as polygons. StarDist [16], a popular approach in this domain, predicts radial distances at equidistant angles from each pixel to the nucleus boundary to form a star-convex polygon. It uses an Euclidean distance map to the nearest background pixel, with Non-Maximum Suppression (NMS) to deduplicate overlapping predictions. This method has also been extended for nuclei classification [17]. CPP-Net [14] improves StarDist by refining the prediction of radial distances, using a weighted average of radial distance predictions from a pixel’s neighbors along the distance rays, leading to more accurate results. SplineDist [30], in contrast, replaces radial distances with splines to describe nuclei contours.

While splines offer advantages like enforced smoothness that better match the natural shapes of nuclei, they lack an orthogonal basis, complicating the loss calculation as differently parametrized splines can represent the same shape. To address this limitation, FourierDist [31] employs Fourier descriptors [32], which have an orthogonal basis and can accurately capture nuclei shapes with fewer parameters than star-convex polygons.

Although these methods are highly effective and achieve state-of-the-art performance on most nuclei segmentation benchmarks, the reliance on per-pixel prediction and handcrafted post-processing methods slows down inference, especially when working with large input images. Additionally, StarDist-based methods struggle with predicting overlapping nuclei due to NMS, while HoVer-Net-based methods cannot predict overlapping nuclei at all.

2.3. DETR-Based Approaches

The closest approaches to set prediction are auto-regressive sequence models, such as recurrent neural networks [33] and transformers [34]. While these models can handle sequential data, they face challenges in batching and increased inference time proportional to the sequence length.

To overcome these limitations, the DEtection TRansformer (DETR) [18] introduces a parallel set prediction approach. DETR employs a fixed set of learnable object queries whose quantity exceeds the maximum number of objects typically found in an image. The network predicts objects for all queries simultaneously but learns to filter the surplus by classifying them as “no object”. This mechanism allows for direct, end-to-end prediction, effectively eliminating the need for heuristic post-processing steps.

The adoption of DETR-based methods in nuclei segmentation is an emerging research direction. Cell-DETR [35] was the first to adapt DETR for nuclei segmentation, predicting a binary mask for each token to represent individual nuclei. NucDETR [12] explored a similar approach but limited its predictions to bounding boxes. ACFormer [10] focuses on predicting nuclei centroids using an affine-consistent transformer framework. This method incorporates a local-global network architecture, where the local network predictions are guided by the global network’s broader contextual understanding, ensuring scale consistency across varying image magnifications.

The most relevant approach to ours is SAP-DETR [36], developed for general object detection using bounding boxes. It introduces query-specific positions by distributing object queries over a fixed mesh grid while allowing

dynamic movement of queries. Our method extends this concept by eliminating the global context requirement, informed by specific characteristics of nuclei, enabling dynamic scaling of object queries based on input size and resolution.

3. LSP-DETR Model

On a high level, the LSP-DETR receives an image as input and outputs a set of shape descriptors representing segmented nuclei, their semantic embeddings, and classes. The model consists of a feature extractor (backbone in DETR terminology) processing the image and a transformer module that operates on shape descriptors and embeddings. The architecture is outlined in Figure 4.

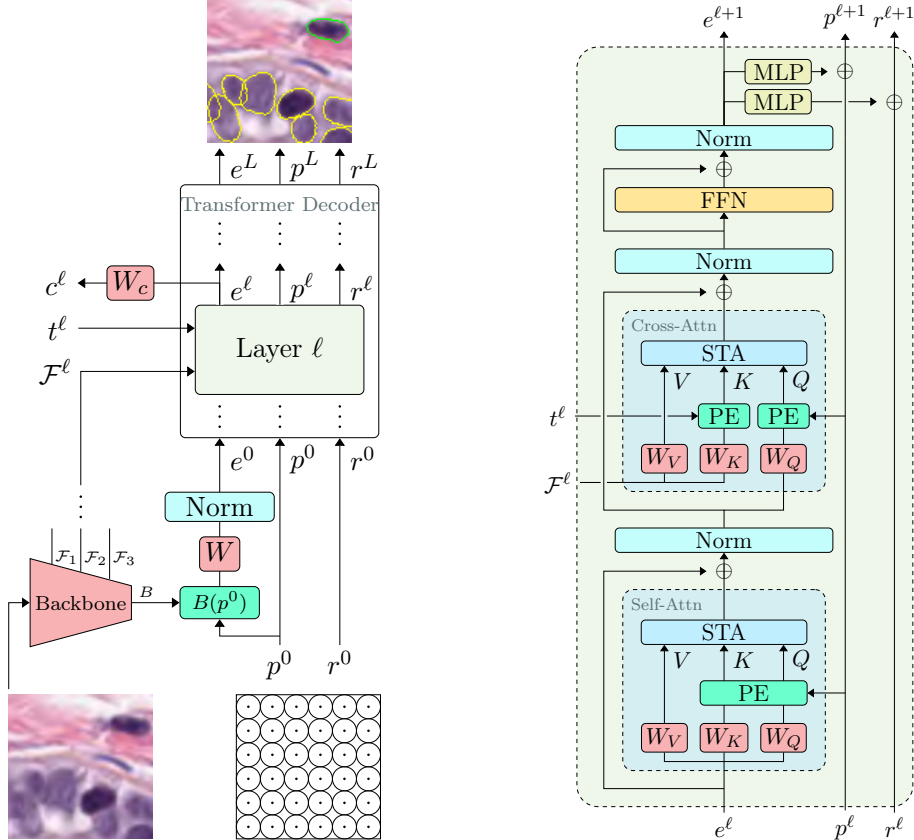
3.1. Visual Feature Extractor

Given a square input image of dimensions $3 \times R \times R$, the backbone extracts several multi-scale features \mathcal{F}_i of size $C_i \times R_i \times R_i$ and a final feature map B , with dimensions $C_B \times R_B \times R_B$. The whole architecture can be straightforwardly generalised to rectangular images, but we stick to the square case for simplicity.

We adopt a transformer-based backbone, motivated by the observation that conventional CNNs, which rely on padding, can introduce minor positional inaccuracies of radial distances when applied to images of varying resolutions. In particular, we employ the widely used and efficient Swin-V2-T [37], a lightweight transformer backbone that is agnostic to input image size. Features \mathcal{F}_1 , \mathcal{F}_2 , \mathcal{F}_3 , and output B correspond to embedding vectors taken after Swin Stages 1-4; see Figure 4a. We fine-tune the model starting from weights pretrained on ImageNet-1K [37]. However, the model is in principle compatible with any locally-based backbone architecture.

3.2. Transformer Module

The transformer operates on N *object queries* $(e_j^\ell, p_j^\ell, r_j^\ell)$ for $j = 1, \dots, N$, with the upper index ℓ indexing the layer. For a query j , the vector $e_j^\ell \in \mathbb{R}^d$ denotes a content embedding, $p_j^\ell \in [0, 1]^2$ is a relative position in the image and $r_j^\ell \in \mathbb{R}_+^{64}$ are radial distances approximating the nucleus shape, as depicted in Figure 3a. We selected 64 rays as in StarDist [17]. We also collect all queries to $e^\ell = (e_1^\ell, \dots, e_N^\ell)$ and similarly for p^ℓ and r^ℓ .



(a) Overall model pipeline. The input image is processed by a Swin-V2-T backbone to extract multi-scale feature maps $\mathcal{F}_1, \mathcal{F}_2, \mathcal{F}_3$, and a final feature map B . Object queries (e^0, p^0, r^0) are initialized as a fixed grid of circular descriptors with positions p^0 and radial distances r^0 . The initial query embeddings e^0 are generated by sampling the backbone output B at the grid positions p^0 . These queries are iteratively refined by the Transformer Decoder to produce final class predictions c^L , positions p^L , and radial distances r^L .

(b) Structure of Transformer Layer ℓ . Query embeddings e^ℓ are updated through a self-attention block (modeling interactions between object queries), a cross-attention block (integrating image features \mathcal{F}^ℓ), and a Feed-Forward Network (FFN). We employ Sliding Tile Attention (STA) for efficient local processing, and rotary Position Encodings (PE) to incorporate geometric information from positions p^ℓ and image feature coordinates t^ℓ . Separate MLP heads predict the updates to the positions $p^{\ell+1}$ and radial distances $r^{\ell+1}$.

Figure 4: The LSP-DETR Architecture.

The initial nuclei descriptors (p^0, r^0) are set to approximations of circles of radius s distributed evenly in a regular grid and tightly packed in the image, as depicted in Figure 4a. The hyperparameter s depends on the image size R (px), resolution ($\mu\text{m}/\text{px}$), and the nuclei biology, roughly representing the relative minimal nucleus radius. While the minimum size of a biological

nucleus is approximately 3 μm [38], we set the initial grid cell diameter to 3.5 μm to ensure adequate separation and localization. The normalized radius s is thus defined as

$$s = \frac{3.5 \mu\text{m}}{2 \times R \times \text{resolution}}. \quad (1)$$

To define e^0 , we take the backbone output B and localize it to the positions p^0 . Specifically, let $B(p_j^0) \in \mathbb{R}^C$ be the pixel value of the backbone output B at the relative position p_j^0 (the bilinear interpolation of neighboring pixels is taken). Now $e^0 = \text{Norm}(WB(p^0))$, where $W \in \mathbb{R}^{d \times C}$ is a linear transform and Norm is a layer normalization.

The object queries are iteratively refined by the *transformer layers* in the *transformed decoder*, see Figure 4a. During the process, the model adjusts the nuclei positions and shapes and updates the information collected in the embeddings. The architecture is designed so that each object query can segment the nucleus in its near surroundings. Therefore, the positions p^ℓ are restricted to remain in the grid cell where they were initiated.

Moreover, as the number of nuclei is overapproximated, the model must have the ability to disregard the entire query. Therefore, we employ a linear classifier that predicts nuclei classes c^ℓ from their embeddings e^ℓ after each layer ℓ of the transformer. The number of classes depends on the task, but there is always at least one class reserved for the “no nucleus” category, denoted by \emptyset , to drop the query in the final set of segmented nuclei.

3.3. Transformer Layers

Our decoder architecture makes two fundamental modifications to the standard transformer layers to improve both efficiency and geometric awareness. First, we replace absolute positional encodings with a unified relative encoding scheme, using the multidimensional Cayley-STRING rotary encodings [39]. This integrates relative spatial information into the attention dot product by rotating the query and key vectors. Second, recognizing that segmentation is an inherently local operation, we replace the standard quadratic-cost full attention with Sliding Tile Attention (STA) [40]. This mechanism efficiently restricts attention to local neighborhoods, achieving linear complexity. The Layer design is outlined in Figure 4b.

Self Attention. In the self-attention layers, each object query is refined by attending to the object queries in its local neighborhood. This neighborhood remains constant across all transformer layers because the positions

are updated to stay within the grid cell where they were initialised. Consequently, the neighborhood is determined by the initial positions p^0 of the object queries. STA is used to efficiently implement this local attention mechanism, providing sufficient context for queries to interact and perform tasks like deduplication.

To encode relative positions (PE), we use Rotary Positional Encodings (RoPE). The query Q_j and key K_j vectors are obtained from the embedding e_j^ℓ of the object query, by applying a rotational matrix corresponding to the position p_j^ℓ as

$$Q_j = \text{RoPE}(p_j^\ell/s)P^\ell W_Q e_j^\ell, \quad (2)$$

and

$$K_j = \text{RoPE}(p_j^\ell/s)P^\ell W_K e_j^\ell. \quad (3)$$

Here, P^ℓ is a learnable orthogonal transformation shared by Q_j and K_j but unique for each layer. Next, RoPE is the two-dimensional rotary positional encoding as in Cayley-STRING [39]. Note that the positions are divided by s to make it scale independent.

Cross Attention. In cross-attention layers, object queries interact with image features. This interaction is also restricted to a fixed neighborhood defined by the queries' initial positions. The query vectors Q_j are derived from the embeddings e_j^ℓ of the object queries the same way as in the self-attention (2).

In contrast, the keys K_j and values V_j are derived from the image feature \mathcal{F}^ℓ . The multi-scale image features are fed from the backbone into the decoder in a round-robin fashion, progressing from the lowest to the highest resolution, i.e., we set $\mathcal{F}^\ell = \mathcal{F}_{\ell \bmod 3}$ in our case. However, we must convert the image features to the same format as the object queries. Therefore, we transform the image feature \mathcal{F}^ℓ of size $C^\ell \times R^\ell \times R^\ell$ to a sequence of embeddings $f_j^\ell \in \mathbb{R}^{C^\ell}$ and relative image positions $t_j^\ell \in [0, 1]^2$.

To this end, we fix a one-to-one mapping (enumeration) between indices j , $(0 \leq j < (R^\ell)^2)$ and feature positions (x, y) for $0 \leq x, y < R^\ell$. Namely, we take $j = R^\ell y + x$, corresponding to flattening. Then we set the key token as the local image feature $f_j^\ell = \mathcal{F}^\ell(x, y) \in \mathbb{R}^{C^\ell}$ and its relative image position as $t_j^\ell = \frac{1}{R^\ell}(x + \frac{1}{2}, y + \frac{1}{2})$. Finally, the keys K_j are given by

$$K_j = \text{RoPE}(t_j^\ell/s)P^\ell W_K f_j^\ell, \quad (4)$$

where, as well as in the self-attention, the learnable orthogonal transform P^ℓ is shared by queries and keys, but is unique for each layer. This encoding

strategy ensures that object queries and image features share a consistent spatial representation, which is critical for aligning them accurately during the attention process.

Prediction Heads. At each layer ℓ , the output embedding e^ℓ of each object query is passed to two prediction heads to update the position p^ℓ and radial distances r^ℓ . A three-layer MLP predicts an offset $\Delta p^\ell \in \mathbb{R}^2$. The positions $p^{\ell+1}$ are then updated from p^ℓ similarly as in SAP-DETR [36], i.e.,

$$p^{\ell+1} = s \tanh(\tanh^{-1}((p^\ell - p^0)/s) + \Delta p^\ell) + p^0, \quad (5)$$

ensuring that the nucleus does not drift away from its original grid position p^0 further away than s . Another three-layer MLP predicts the change in radial distances $\Delta r^\ell \in \mathbb{R}^{64}$, updating the radial distances as $r^{\ell+1} = r^\ell \exp(\Delta r^\ell)$.

3.4. Set Prediction Loss

Our model formulates instance segmentation as a direct set prediction task, outputting final instances without the need for post-processing. Consequently, the loss computation is a two-step process: first, an optimal bipartite matching assigns each ground-truth nucleus to the best-fitting prediction, and second, a loss function penalizes the dissimilarities within these assigned pairs. The loss and matching processes are performed at each decoder layer with “look forward twice” scheme as in [41], therefore, we omit the layer index ℓ from the predictions in this section for brevity.

The total loss is designed to optimize two primary objectives: accurate nuclei classification and high-fidelity shape reconstruction. We encourage faithful shape modeling by training the network to predict the points p near the nucleus centroid. This approach is based on the assumption that radial distances from a central point are more likely to effectively parameterize nuclei shapes.

To handle the assignment between predictions and ground-truth instances, we adopt the bipartite matching strategy used in DETR. Let the ground-truth set consist of M nuclei, where the j -th nucleus is represented by its class label \bar{c}_j and binary instance mask $\bar{m}_j \in \{0, 1\}^{R \times R}$. From the mask, we compute the ground-truth nucleus centroid \bar{p}_j . The model outputs N predictions, where N corresponds to the number of grid cells and therefore varies with the input image’s dimensions. The grid density is chosen to ensure $N \geq M$. Each prediction j consists of a class score c_j , predicted point p_j , and a vector of radial distances r_j .

Bipartite Matching. The core of our method is to find an optimal one-to-one assignment between the M ground-truth nuclei and the N predictions. We find the optimal assignment σ^* , within all M -permutations of N elements $\sigma: \{1, \dots, M\} \rightarrow \{1, \dots, N\}$, by minimizing the pairwise matching cost

$$\mathcal{W}(\sigma) = \sum_{j=1}^M \mathcal{W}_c(\bar{c}_j, c_{\sigma(j)}) + \mathcal{L}_p(\bar{p}_j, p_{\sigma(j)}) + \mathcal{L}_r(p_{\sigma(j)}, r_{\sigma(j)}) + \mathcal{W}_m(\bar{m}_j, p_{\sigma(j)}), \quad (6)$$

where the classification loss \mathcal{W}_c is the custom modification of the focal loss taken exactly as in [41] (including hyperparameters). The term \mathcal{L}_p is the L^1 distance between the ground-truth nucleus centroid \bar{p}_j and the predicted point $p_{\sigma(j)}$. Next, \mathcal{L}_r is our proposed radial distance loss, detailed below, and \mathcal{W}_m is an inner mask cost discouraging predicting the positions outside the nucleus, defined by

$$\mathcal{W}_m(m, p) = \begin{cases} 0 & \text{if the point } p \text{ lies inside the mask } m, \\ \lambda & \text{otherwise.} \end{cases} \quad (7)$$

The weight λ is set so that the misassignment of the position $p_{\sigma(j)}$ to the ground-truth mask \bar{m}_j dominates the other cost components, e.g. $\lambda = 10$. The optimal assignment is found efficiently using a GPU-accelerated linear assignment solver [42].

Loss Function. After determining the optimal assignment σ^* , the final loss is computed as a sum of shape reconstruction losses over the matched pairs and a classification loss over all predictions

$$\begin{aligned} \mathcal{L} = & \frac{1}{N} \sum_{j=1}^M \mathcal{L}_c(\bar{c}_j, c_{\sigma^*(j)}) + \frac{1}{N} \sum_{\substack{1 \leq k \leq N \\ k \notin \text{Range}(\sigma^*)}} \mathcal{L}_c(\emptyset, c_k) \\ & + \frac{1}{M} \sum_{j=1}^M [\mathcal{L}_p(\bar{p}_j, p_{\sigma^*(j)}) + \mathcal{L}_r(p_{\sigma^*(j)}, r_{\sigma^*(j)})]. \end{aligned} \quad (8)$$

The classification loss \mathcal{L}_c is the standard focal loss [43]. It is applied to all N predictions so that for the M matched predictions, the target is the corresponding ground-truth class \bar{c}_j , and for the remaining $N - M$ unmatched predictions ($k \notin \text{Range}(\sigma^*)$), the target is the “no nucleus” (\emptyset) class. The point loss \mathcal{L}_p and radial loss \mathcal{L}_r are only computed for the M matched pairs.

Radial Distance Loss. The radial distance loss \mathcal{L}_r is designed to effectively supervise the prediction of radial distances while addressing several key challenges. A naive approach, such as a direct L^1 loss between predicted distances and a single ground-truth vector, is impractical. First, on-the-fly computation or pre-storage of precise ground-truth distances is computationally and memory-intensive. Second, in domains such as nuclei segmentation, ground-truth masks often feature overlapping instances where the overlapping regions are not explicitly annotated. A standard loss would incorrectly penalize a model for predicting these physically plausible overlaps. Our approach avoids this by design.

To overcome these limitations, we propose a loss that penalizes predictions only when they fall outside a plausible range, rather than enforcing a single exact value. This range is defined by a lower and an upper bound. Crucially, these bounds and the subsequent loss are only computed for positions p_j that lie inside any ground-truth nucleus mask \bar{m} . We call these positions *foreground points*. All the remaining points are ignored by the loss function.

Let r be the vector of 64 predicted radial distances of a foreground point p . We define the *lower bound* $r_{\min} \in \mathbb{R}^{64}$ as a vector of radial distances from p to the nearest edge of any ground-truth mask containing p , or to the image boundary. Next, we set *upper bound* $r_{\max} \in \mathbb{R}^{64}$ as a vector of radial distances from p to nearest pixels that are not covered by any ground-truth nucleus mask. If the whole ray is covered by the ground-truth masks up to the image boundary, we set r_{\max} to infinity. For illustration, see Fig. 5.

Finally, the loss is zero for any predicted distance that lies within its respective bounds $[p_{\min}, p_{\max}]$ and incurs a penalty proportional to the violation otherwise. Namely, we set

$$\mathcal{L}_r(p, r) = \frac{1}{64} \sum_{k=1}^{64} \max \{r_{\min} - r, 0, r - r_{\max}\}_k, \quad (9)$$

where the maximum is considered elementwise. This design is highly efficient because both the lower and upper bound vectors can be precomputed for each pixel, independent of the number of instances in an image. Furthermore, it robustly handles object overlaps and annotation ambiguities by only penalizing demonstrably incorrect predictions.

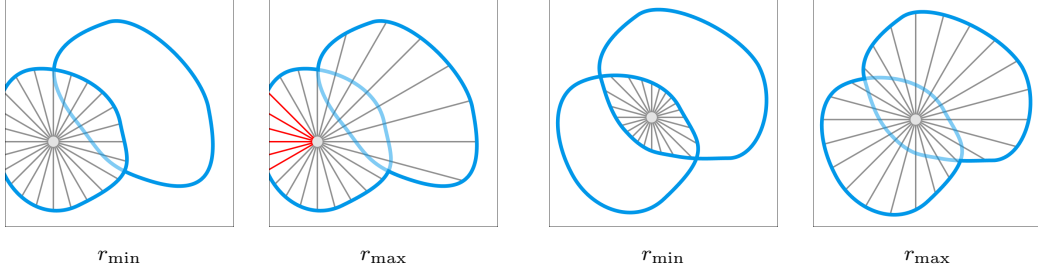


Figure 5: Visualization of the lower bound r_{\min} and upper bound r_{\max} for radial distances originating from a point p (gray dot). Ground-truth nuclei are delineated by blue outlines. The scenarios are organized into two groups: (left) a point within a nucleus near the image boundary, and (right) a point within an overlapping region. Red rays signify an infinite distance bound, occurring when a ray does not intersect a background pixel within the image frame.

3.5. Evaluation Metrics

We assess model performance on two distinct tasks: instance segmentation and instance detection. For consistency and fair comparison, we adopt the primary metrics and matching criteria used in CellVit [11].

Let $\bar{m}_1, \dots, \bar{m}_M$ denote the ground-truth instance masks. Similarly, let m_1, \dots, m_N represent the instance masks obtained by rasterizing predicted star-convex polygons, with c_1, \dots, c_N be their predicted classes from K classes.

Instance Segmentation. We quantify instance segmentation quality using a unified metric called *Panoptic Quality* (PQ) [44] which captures both segmentation and detection quality. The evaluation process begins by matching predictions to ground-truth instances of the same class. For each class, we find an optimal bipartite matching between the sets of ground-truth and predicted masks that maximizes the total Intersection over Union (IoU).

Based on this matching and an IoU threshold of 0.5, instances are categorized. We define *True Positives* (TP) as the set of matched pairs (\bar{m}, m) where $\text{IoU}(\bar{m}, m) > 0.5$, *False Positives* (FP) as the set of predicted instances m that are not part of any matched pair, and *False Negatives* (FN) as the ground-truth instances \bar{m} that are not part of any matched pair. For a class c , we compute *Segmentation Quality* (SQ_c) and *Recognition Quality* (RC_c) as

$$\text{SQ}_c = \frac{1}{|\text{TP}|} \sum_{(\bar{m}, m) \in \text{TP}} \text{IoU}(\bar{m}, m), \quad \text{RC}_c = \frac{|\text{TP}|}{|\text{TP}| + \frac{1}{2}|\text{FP}| + \frac{1}{2}|\text{FN}|}, \quad (10)$$

and finally, the Panoptic Quality as their product $\text{PQ}_c = \text{SQ}_c \cdot \text{RC}_c$.

To provide a comprehensive evaluation, we report two versions of this metric. First, *Multi-class Panoptic Quality* (mPQ) evaluates the model’s per-class performance by calculating PQ_c for each of the K classes independently and then reports the average

$$\text{mPQ} = \frac{1}{K} \sum_{c=1}^K \text{PQ}_c. \quad (11)$$

Second, *Binary Panoptic Quality* (bPQ) assesses the model’s overall ability to identify instances, regardless of their type. It is calculated by treating all the classes as a single one before performing the matching and calculation.

Fair Evaluation of Overlapping Nuclei. A key advantage of our method is its ability to predict realistic, overlapping nuclei. However, ground-truth annotations in standard benchmarks enforce strict, often artificial separation between touching instances. Standard PQ metrics rigidly penalize predictions that cross these boundaries, treating biological overlaps as false positives. Furthermore, attempting to resolve these overlaps via post-processing often results in incorrect instance separations that deviate from the ground truth.

To resolve this, we propose the *Masked Panoptic Quality* (MPQ), a modification of PQ designed for this specific scenario. MPQ uses the same core formula but replaces the standard IoU with a masked IoU (mIoU) that isolates the evaluation to the matched ground-truth instance. Specifically, the mIoU is defined as

$$\text{mIoU}(\bar{m}, m) = \frac{|\bar{m} \cap m|}{|\bar{m} \cup (m \setminus G)|}, \quad (12)$$

where $G = \bigcup_{k=1}^m \bar{m}_k$ is the union of all ground-truth masks. Instead of including the entire area of the prediction m , it only considers the area of the ground-truth mask \bar{m} plus any part of the prediction that falls outside of G . Compare with IoU, where the denominator is $|\bar{m} \cup m|$.

Instance Detection. Following Sirinukunwattana et al. [45], a predicted instance is matched to a ground-truth instance if the Euclidean distance between their respective centroids is less than or equal 3 μm . Each ground-truth object can be matched at most once. To evaluate the model’s ability to correctly localize nuclei, we use the standard detection metrics of F_1 score, *Precision* (P), and *Recall* (R).

4. Experiments

4.1. Datasets

To train and evaluate our models, we use several publicly available datasets, each comprising H&E-stained RGB images paired with per-nucleus pixel-level segmentation masks. These datasets provide a diverse range of samples, covering various tissue types, staining variations, and nuclei characteristics.

PanNuke. Our primary dataset for training and evaluation is PanNuke Gamper et al. [20, 46]. It consists of 7,901 images, each sized 256×256 px, collectively containing 189,744 annotated nuclei. Crucially, these nuclei annotations are strictly non-overlapping, meaning the annotations do not model spatial overlap or occlusion between nuclear instances. All images were captured at $\times 40$ magnification, corresponding to a resolution of $0.25 \mu\text{m}/\text{px}$. The dataset is highly diverse, featuring samples from 19 different tissue types and classifying nuclei into five categories: neoplastic, inflammatory, dead, epithelial, and connective/soft cells.

MoNuSeg. To evaluate segmentation generalization, we utilize the test set from the MoNuSeg dataset [47, 9]. This set contains 14 images with 7,223 annotated nuclei, sourced from seven different organs. While the images share the same $\times 40$ magnification ($0.25 \mu\text{m}/\text{px}$ resolution) as PanNuke, they are significantly larger (1000×1000 px). Importantly, the nuclei in MoNuSeg are not categorized by cell type. Unlike PanNuke’s strictly non-overlapping masks, some instances in MoNuSeg share small overlapping regions. However, these overlaps are artifacts of the manual delineation process rather than an intentional modeling of nuclear occlusion.

TCGA. We evaluate the computational performance of our model on WSIs selected from the TCGA-COAD/READ cohort. To ensure a direct comparison, we used the same set of images as the HoVer-NeXt benchmark [19].² This set includes images with tissue sizes ranging from 20 mm^2 to 500 mm^2 (estimated using their algorithm), with further details provided in Tab. 2.

4.2. Experimental Setup

Input Preprocessing. To standardize the input data, we normalize the RGB channels of each image using a mean $\mu = [0.485, 0.456, 0.406]$ and a std $\sigma = [0.229, 0.224, 0.225]$, consistent with the ImageNet pretraining of the backbone. We do not apply cropping, tiling, or padding in our experiments,

Table 2: Representative images from the TCGA-COAD/READ cohort used for inference speed evaluation. To ensure direct comparison, we used the same set of images and tissue area estimation as Baumann et al. [19].

Case ID	Slide ID	H×W (px)	μm/px	mm ²
TCGA-AA-3977	DX1	57,600×34,560	0.2325	20.16
TCGA-AA-3688	DX1	101,120×66,816	0.2325	49.84
TCGA-AA-A010	DX1	68,352×71,424	0.2325	101.09
TCGA-CK-4951	DX1	64,833×94,965	0.2520	202.90
TCGA-5M-AAT5	DX1	89,145×161,352	0.2525	501.00

as LSP-DETR supports processing images of arbitrary size. Consequently, all evaluations are performed on full-resolution images.

To efficiently find the ground-truth radial distance bounds (r_{\min} and r_{\max}) for any point p , our method relies on two precomputed lookup tables. We generate these tables (one for r_{\min} and one for r_{\max}) using a custom algorithm inspired by the methodology in StarDist [16]. For each pixel in the $R \times R$ image, this algorithm measures the distance to the object’s boundary along 64 fixed radial directions. The minimum and maximum of these 64 distances are then stored in their respective tables. Once the tables are built, finding the bounds for any point p becomes a simple lookup at its coordinates. For points that fall between pixels, we use bilinear interpolation to calculate a smooth average from the surrounding pixel values.

Model Hyperparameter Settings. Following DETR, our transformer module uses a post-layer normalization transformer. The model is configured with a token dimension of $d = 384$, $L = 6$ transformer layers with 12 attention heads, and a SwiGLU-based feed-forward network ($\text{FFN}_{\text{SwiGLU}}$) [48] with an intermediate dimension of 1024.

We employ STA [40] for all attention layers. For self-attention, we use a 3×3 tile size for object queries with an attention window of 3 to facilitate deduplication. In cross-attention, while the queries retain their 3×3 tile size, we widen the attention window to 5 to better capture large nuclei from the multi-scale image feature maps, which are tiled at 2×2 , 4×4 , and 8×8 for resolutions $1/16$, $1/8$, and $1/4$, respectively. Finally, we use the RoPE with learnable frequencies initialized with a base of $\theta = 100$.

Training. To ensure a fair comparison, our training regimen closely follows that of Cell-ViT [11]. Models are trained for 130 epochs with a batch size of 16, adopting their staged approach: the backbone weights are frozen for the first 30 epochs and subsequently fine-tuned with a learning rate set to 10% of the main learning rate. Furthermore, we use the same data augmentation and sampling strategies as described in their work.

For optimization, we use the AdamW optimizer [49] with an initial learning rate of 10^{-4} and a weight decay of 10^{-4} . The learning rate is managed by a cosine annealing schedule with a 10-epoch linear warm-up. To improve efficiency, we employ float16 mixed precision and apply gradient norm clipping with a threshold of 0.1. FLOPs are measured on a single 256×256 input image with a resolution of $0.25 \mu\text{m}/\text{px}$.

Baseline Methods. To ensure a fair and comprehensive comparison, we utilized the highest-performing variants of state-of-the-art methods. For CellViT [11], we employed the CellViT-SAM-H version. We evaluated LKCell [15] using its large variant, LKCell-L. For HoVer-NeXt [19], we selected the $\text{HN}_{\text{Tiny},16\text{TTA}}$ configuration, as it offers a strong balance of speed and accuracy. Finally, CPP-Net [14] was evaluated with a ResNet50 [50] backbone.

Inference and Evaluation. We apply a deterministic distance-transform watershed refinement specifically for evaluations on the PanNuke dataset. This is required by two factors: PanNuke annotations are strictly non-overlapping, and the standard Panoptic Quality (PQ) metric forbids overlapping predictions. This refinement resolves overlaps by assigning shared pixels to the instance with the largest Euclidean distance from its boundary.

The inference speed benchmarks were executed on a system equipped with 12 CPUs, 64 GB RAM, and an NVIDIA H100 NVL GPU. For LKCell, StarDist, and CPP-Net, measurements were obtained using our optimized multi-processing pipeline. The implementation of CPP-Net was taken from CellSeg Models [51], while HoVer-NeXt was evaluated using its official implementation. The runtime of CellViT was approximated from the results reported in the HoVer-NeXt paper [19].

4.3. Results

Evaluation on the PanNuke Dataset. We follow the standard three-fold cross-validation as described in [4]. For evaluation, we use the final training checkpoint from each of the three folds to avoid selection bias, and all reported metrics represent the average performance across the three folds.

Table 3: Performance of instance segmentation on the PanNuke dataset across the 19 tissue types using three-fold cross-validation. The standard deviation (STD) across the three splits is provided in the final row. The best results among bPQ and mPQ are highlighted. StarDist was trained by Chen et al. [14].

Tissue	HoVer-NeXt		StarDist		CPP-Net		CellViT		LKCell		LSP-DETR	
	mPQ	bPQ	mPQ	bPQ	mPQ	bPQ	mPQ	bPQ	mPQ	bPQ	mPQ	bPQ
Adrenal	49.4	70.4	48.7	69.7	49.4	70.7	51.3	70.9	50.8	71.3	47.1	70.9
Bile Duct	46.8	66.8	46.5	66.9	46.7	67.7	48.9	67.8	48.9	68.2	46.3	67.2
Bladder	57.8	69.6	57.9	69.9	59.4	70.5	58.4	70.7	59.9	71.5	58.3	71.1
Breast	49.5	64.3	50.6	66.7	50.9	67.5	51.8	67.5	51.4	66.9	51.4	67.6
Cervix	47.5	66.7	46.3	66.9	47.9	69.1	49.8	68.7	49.9	69.6	49.3	68.8
Colon	42.8	57.0	42.1	57.8	43.2	59.1	44.9	59.2	45.6	59.4	44.4	59.6
Esophagus	52.7	64.7	53.3	66.6	54.5	68.0	54.5	66.8	56.1	68.3	54.3	67.7
Head&Neck	48.5	64.3	47.7	64.3	47.1	65.2	49.1	65.4	50.0	66.1	48.4	64.8
Kidney	51.7	68.3	48.8	70.0	51.9	70.7	53.7	70.9	55.8	72.0	52.4	69.9
Liver	50.4	71.7	51.5	72.3	51.4	73.1	52.2	73.2	53.0	73.7	49.8	72.1
Lung	42.9	63.4	41.3	63.6	42.6	63.9	43.1	64.3	43.1	64.9	42.9	64.0
Ovarian	48.6	61.2	52.1	66.7	53.1	68.3	53.9	67.2	54.4	67.6	51.6	67.6
Pancreatic	46.0	65.7	45.9	66.0	47.1	67.9	47.2	66.6	49.0	67.7	47.9	67.1
Prostate	48.1	62.9	50.7	67.5	53.1	69.0	53.2	68.2	52.3	68.1	51.6	67.5
Skin	41.4	62.3	36.1	62.9	35.7	62.1	43.4	65.7	40.8	66.0	37.7	64.1
Stomach	46.1	69.6	44.8	69.4	45.8	70.7	47.1	70.2	46.6	71.5	43.7	68.7
Testis	49.7	68.0	49.4	68.7	49.3	70.3	51.3	69.6	53.5	69.4	48.7	68.7
Thyroid	42.2	67.7	43.0	69.6	43.9	71.6	45.2	71.5	46.6	71.5	44.8	70.3
Uterus	44.6	61.9	44.8	66.0	47.9	66.2	47.4	66.3	49.0	66.6	45.9	64.8
Average	47.7	65.6	47.4	66.9	48.5	68.0	49.8	67.9	50.3	68.4	48.2	67.5
STD	—	—	—	—	—	—	0.77	0.39	0.96	0.25	0.83	0.24

Tab. 3 provides a comprehensive comparison of panoptic quality across 19 tissue types using bPQ and mPQ metrics. Notably, the LKCell metrics reported in these tables were recomputed from official result logs to resolve discrepancies in the original publication and ensure a fair comparison.

We also report MPQ scores (Sec. 3.5) to account for the artifacts of watershed refinement, where instance separation may incorrectly shift boundaries relative to the ground truth. This metric effectively softens the boundaries between touching ground-truth nuclei, allowing us to assess performance without the unfair penalty against realistic overlaps. LSP-DETR achieves an average mMPQ of 49.0 and a bMPQ of 68.8, ranking first in binary mask quality. While we cannot re-evaluate other methods using MPQ due to the lack of raw predictions or pretrained checkpoints, their MPQ and PQ scores are expected to be nearly identical. This is because MPQ differs from standard PQ only in regions with dense nuclei annotations, where existing

Table 4: Comparison of Panoptic Quality (PQ) for each cell category on the PanNuke dataset. The PQ scores are averaged across the three-fold cross-validation.

Model	Neoplastic	Inflammatory	Dead	Connective	Epithelial
HoVer-NeXt	53.6	41.8	15.4	41.5	51.5
CellViT	58.1	41.7	14.9	42.3	58.3
LKCell	58.4	43.7	15.5	42.5	58.5
LSP-DETR	57.4	41.3	13.0	40.8	54.5

Table 5: Performance of detection scores across individual PanNuke categories. The scores are averaged across the three-fold cross-validation.

Model	Neoplastic			Inflammatory			Dead			Connective			Epithelial		
	P	R	F ₁	P	R	F ₁	P	R	F ₁	P	R	F ₁	P	R	F ₁
HoVer-NeXt	-	-	72.0	-	-	68.1	-	-	49.2	-	-	64.6	-	-	72.8
CellViT	71.8	69.3	70.5	59.3	57.4	58.3	43.0	31.6	36.3	54.5	52.5	53.5	72.4	73.2	72.8
LKCell	70.3	71.7	71.0	58.2	59.9	59.0	45.3	34.5	39.1	57.3	50.2	53.5	74.0	75.5	74.7
LSP-DETR	76.9	73.2	75.0	71.1	68.4	69.7	59.4	39.8	47.4	66.8	59.1	62.7	77.2	73.6	75.4

methods are trained to precisely reconstruct the ground-truth boundaries of touching nuclei.

We further analyze performance across PanNuke’s five distinct cell categories. Tab. 4 compares the panoptic quality for each cell type using the aforementioned watershed refinement, while Tab. 5 isolates detection performance, reporting detection quality metrics for each individual cell category.

Evaluation on the MoNuSeg Dataset.

To assess generalization and scalability, we evaluated our PanNuke-trained models (from all three cross-validation folds) directly on the MoNuSeg test set. This evaluation highlights our model’s input-size agnosticism: despite being trained exclusively on 256×256 px patches, our method processes the entire 1000×1000 px MoNuSeg images at inference. This is achieved in a single pass, eliminating the need for the overlapping patch-based strategies required by many other methods.

The results are reported in Tab. 6. As MoNuSeg does not provide cell-

Table 6: Generalization performance of models pretrained on PanNuke and evaluated on the MoNuSeg test set. Averages across three models from a three-fold cross-validation are reported.

Model	bPQ	P	R	F ₁
CellViT	67.2	84.7	88.5	86.5
LKCell	-	-	-	83.0
LSP-DETR	66.7	84.4	85.6	85.0

type labels, the predicted cell category was ignored during this evaluation.

Computational Performance Evaluation on TCGA Dataset. The most significant advantage of LSP-DETR is its computational efficiency, as summarized in Tab. 1. Unlike the other evaluated methods, LSP-DETR is a fully end-to-end model that completely eliminates the need for expensive post-processing. On the TCGA dataset, LSP-DETR achieves an inference speed of 0.46 s/mm^2 , more than $5\times$ faster than the next-fastest model, HoVer-NeXt (2.38 s/mm^2), and $9\times$ faster than LKCell (4.39 s/mm^2).

5. Discussion

Our results demonstrate that LSP-DETR is a highly effective and computationally efficient method for nuclei segmentation. Evaluation across the PanNuke, MoNuSeg, and TCGA datasets highlights four core advantages: robust segmentation and detection performance, strong generalization, strictly better than state-of-the-art inference speed, and the ability to model realistic nuclear overlaps.

5.1. Performance on PanNuke

We first evaluated our method on the PanNuke dataset using standard metrics. Because the standard Panoptic Quality (PQ) metric penalizes overlaps—and PanNuke annotations are strictly non-overlapping—we applied a deterministic distance-transform watershed refinement during inference to resolve overlaps. Under these conditions, LSP-DETR achieves competitive results (48.2 mPQ, 67.5 bPQ), placing it among top-tier methods, though slightly behind LKCell (50.3 mPQ, 68.4 bPQ).

However, this comparison is constrained by a fundamental limitation in the ground truth: PanNuke annotations explicitly forbid biologically realistic overlaps. When evaluated under our proposed overlap-insensitive metrics (mMPQ, bMPQ), which remove this structural bias, LSP-DETR ranks first in binary mask quality (68.8 bMPQ) and remains highly competitive in multi-class quality (49.0 mMPQ).

A closer examination of the category-level performance reveals a notable divergence between our detection scores and segmentation quality. While LSP-DETR achieves the highest detection F_1 -score across all five PanNuke cell categories (Tab. 5), this does not translate to the highest category-specific PQ (Tab. 4). This difference is explained by the distinct aggregation methods

used for each metric and watershed post-processing required to satisfy the non-overlapping constraint.

The F_1 -score is micro-averaged: all true positive (TP), false positive (FP), and false negative (FN) detections from the entire test set are aggregated into global sums before the F_1 -score is computed. This approach weights the final score by the performance on each individual nucleus, meaning that high-density images contribute more to the final score.

By contrast, the per-category PQ is macro-averaged: the metric is calculated independently for each image, and the final result is the arithmetic mean of these per-image scores. This method gives equal weight to every image, regardless of the number of nuclei it contains, placing a greater emphasis on consistent performance across the entire dataset, including sparse or low-density samples.

This behavior is consistent with the training objective: the DETR-style loss function is normalized by the total number of instances within each mini-batch, mirroring the micro-averaging principle by naturally prioritizing high-density samples. The metric divergence, therefore, reflects a real optimization bias in current DETR-style training procedures.

5.2. Generalization to MoNuSeg

A key feature of LSP-DETR is its input-size agnosticism (Tab. 1): despite being trained exclusively on small 256×256 px patches, the model successfully processes full-sized 1000×1000 px MoNuSeg images in a single forward pass.

This evaluation highlights the strong generalizability of our model. While LKCell achieved the highest performance on the PanNuke benchmark (Tab. 3), its performance drops when transferring to MoNuSeg, where it achieves an F_1 -score of 83.0. In contrast, LSP-DETR demonstrates superior robustness, outperforming LKCell with an F_1 -score of 85.0 and maintaining performance levels comparable to the much larger CellViT model (86.5 F_1).

5.3. Computational Efficiency and Scalability

The remarkable efficiency of our method is supported by a lightweight architecture (Tab. 7): LSP-DETR has only 45M parameters and 26G FLOPs, substantially smaller than LKCell (163.8M) and CellViT (699.7M). Furthermore, our method achieves linear complexity and generalization to larger image resolutions—properties most transformer-based architectures (e.g., CellViT) lack due to quadratic attention cost and absolute positional encodings. While convolutional methods can process arbitrary image sizes, their reliance

Table 7: Comparison of the models and computational complexity. *FLOPs were measured using a full attention layer, as the PyTorch flex attention implementation lacks a FLOPs counter. By n we denote the input size (e.g., number of pixels), k is the number of predicted nuclei instances.

Method	# Params	FLOPs	Complexity
StarDist	32.3M	35G	$\mathcal{O}(n + k^2)$
CPP-Net	34.7M	30G	$\mathcal{O}(n + k^2)$
HoVer-NeXt	36.1M	24G	$\mathcal{O}(n \log(n) + kn)$
LKCell	699.7M	214G	$\mathcal{O}(n \log(n) + kn)$
CellViT	163.8M	48G	$\mathcal{O}(n^2)$
LSP-DETR	45.0M	26G*	$\mathcal{O}(n)$

on computationally expensive post-processing algorithms (with $\mathcal{O}(n \log n)$ complexity at best) makes them impractical for processing large WSIs efficiently. This allows inference on images up to 8192×8192 resolution on a single NVIDIA H100 NVL GPU, making it practical for high-throughput WSI pipelines.

5.4. Biologically Realistic Overlap Modeling

To the best of our knowledge, LSP-DETR is the first method that enables biologically correct modeling of nucleus overlaps without requiring explicit overlap annotations during training, which is a significant advantage given the prevalence of overlapping cell structures in real tissue. A major limitation in computational pathology is the lack of datasets with precise, pixel-level annotations for overlapping instances; standard ground-truth masks are artificially separated. Consequently, it is impossible to quantitatively evaluate overlap segmentation with standard metrics.

Despite this limitation, qualitative evaluation confirms that LSP-DETR effectively models biologically realistic overlaps. According to the assessment by the very experienced senior pathologist (R. Nenutil), the model’s ability to identify touching and overlapping nuclei is remarkably good and represents a valuable feature for clinical workflows, although performance naturally varies with tissue quality and staining contrast. An example of this capability is visualized in Fig. 6, where the model successfully delineates overlapping instances (green highlights) that would typically be merged or artificially split by traditional methods.

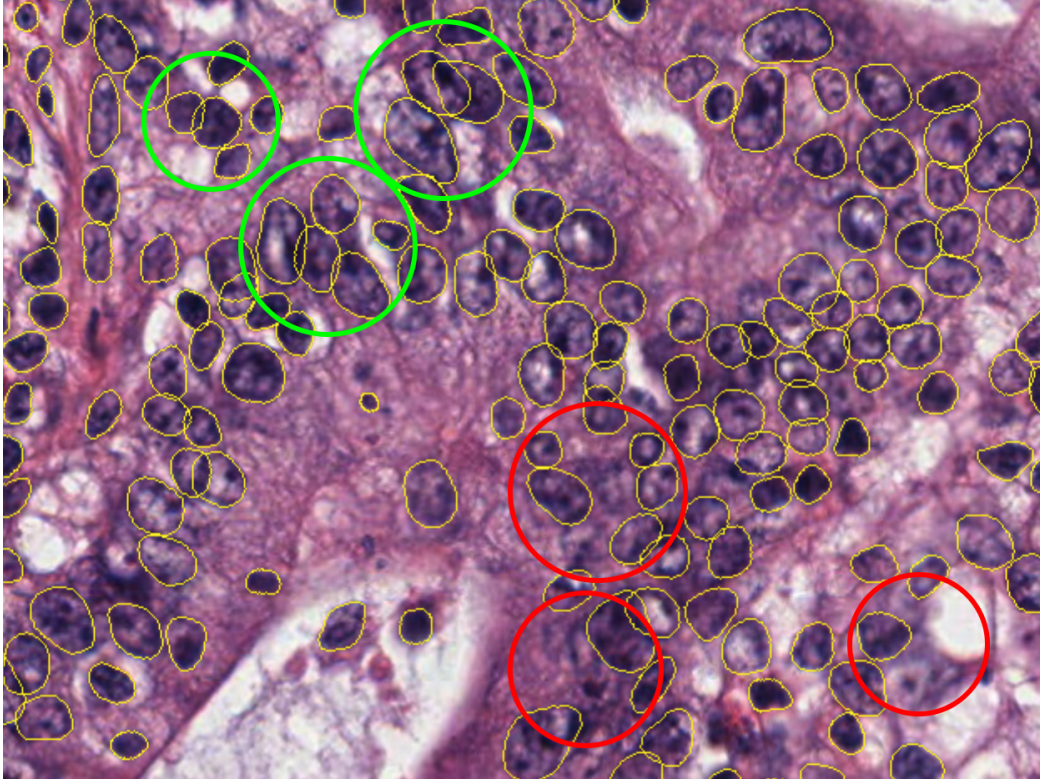


Figure 6: Performance of model in a H&E slide of colon cancer of average quality. The model is able, at least in part, to identify overlapping nuclei (green labels) but fails in areas exhibiting poor focus or contrast with barely identifiable nuclear borders (red labels).

Ablation on Overlap Modeling. We evaluated the impact of our novel radial distance loss compared to the standard approach used by existing methods, which typically penalizes any instance overlap during training. This “standard” behavior is simulated within our framework by setting $r_{\max} = r_{\min}$, effectively forcing the model to converge on a single, precise boundary rather than a plausible range. As shown in Tab. 8, enforcing this penalty leads to lower segmentation accuracy even on strictly non-overlapping PanNuke.

6. Conclusions

In this work, we introduced LSP-DETR, a novel and fully end-to-end framework for cell nuclei instance segmentation. By reimaging nuclei segmentation as a direct set prediction task and representing nuclei as star-convex

Table 8: Ablation study on radial distance modeling on the PanNuke dataset. The “Fixed Boundary” setting simulates standard methods by enforcing $r_{\max} = r_{\min}$. The “Flexible Range” setting uses our proposed radial distance loss to allow for natural overlaps.

Radial Modeling	mPQ	bPQ	mMPQ	bMPQ
Flexible Range (ours)	48.2	67.5	49.0	68.8
Fixed Boundary	47.2	67.1	47.8	68.0

polygons, we have eliminated the need for the computationally expensive and handcrafted post-processing steps that have long hindered the scalability of digital pathology workflows.

Our experimental results on the PanNuke, MoNuSeg, and TCGA datasets demonstrate that LSP-DETR is a highly effective and efficient solution:

State-of-the-Art Efficiency. With an inference speed of 0.46 s/mm² and linear computational complexity, our model is more than 5 times faster than the next-fastest leading method.

Biologically Realistic Modeling. Through our novel radial distance loss, the model naturally learns to segment overlapping nuclei—a common occurrence in real tissue—without requiring explicit overlap annotations during training.

Input-Size Agnosticism. The model demonstrates strong generalization, successfully processing large-scale images in a single forward pass despite being trained on smaller patches.

In conclusion, LSP-DETR bridges the gap between high-fidelity segmentation and practical clinical requirements, setting a new direction in nuclei segmentation through direct instance modeling.

Compliance with Ethical Standards

Acknowledgements

This work has been supported by the AI infrastructure developed in the BioMedAI TWINNING project, supported by EU Horizon Europe, grant agreement no. 101079183. CERIT-SC computational resources were provided by the e-INFRA CZ project (ID:90140), supported by the Ministry of Education, Youth, and Sports of the Czech Republic.

Declaration of generative AI and AI-assisted technologies in the manuscript preparation process

During the preparation of this work, the authors used ChatGPT and Gemini in order to improve the formulation and fluency of the text. Additionally, GitHub Copilot was used to assist with code development and optimization. After using these tools, the authors reviewed and edited the content as needed and take full responsibility for the content of the published article.

References

- [1] V. Magoulianitis, C. A. Alexander, C.-C. J. Kuo, A comprehensive overview of computational nuclei segmentation methods in digital pathology, *APSIPA Transactions on Signal and Information Processing* 12 (2024) –. URL: <http://dx.doi.org/10.1561/116.00000157>. doi:[10.1561/116.00000157](https://doi.org/10.1561/116.00000157).
- [2] S. Brussee, G. Buzzanca, A. M. Schrader, J. Kers, Graph neural networks in histopathology: Emerging trends and future directions, *Medical Image Analysis* 101 (2025) 103444. URL: <https://www.sciencedirect.com/science/article/pii/S1361841524003694>. doi:<https://doi.org/10.1016/j.media.2024.103444>.
- [3] S. Mehta, C. Mercan, J. Bartlett, D. Weaver, J. G. Elmore, L. G. Shapiro, Net-nn: A survey of deep learning methods for cell nucleus segmentation in digital pathology images, *Medical Image Analysis* 67 (2021) 101846.
- [4] S. Graham, Q. D. Vu, S. E. A. Raza, A. Azam, Y. W. Tsang, J. T. Kwak, N. M. Rajpoot, Hover-net: Simultaneous segmentation and classification of nuclei in multi-tissue histology images, *Medical Image Analysis* 58 (2019) 101563.
- [5] Z. Zhang, J. Li, X. Xu, et al., A survey on deep learning methods for histopathology image segmentation: From classical to state-of-the-art models, *Medical Image Analysis* 74 (2022) 102439.
- [6] M. Veta, P. J. van Diest, S. M. Willems, H. Wang, A. Madabhushi, A. Cruz-Roa, F. Gonzalez, A. B. Larsen, J. S. Vestergaard, A. B. Dahl, et al., Automatic nuclei segmentation in h&e stained breast cancer histopathology images, *PloS one* 8 (2013) e70221.

- [7] S. Bhattacharjee, K. Ikromjanov, K. S. Carole, N. Madusanka, N.-H. Cho, Y.-B. Hwang, R. I. Sumon, H.-C. Kim, H.-K. Choi, Cluster analysis of cell nuclei in h&e-stained histological sections of prostate cancer and classification based on traditional and modern artificial intelligence techniques, *Diagnostics* 12 (2021) 15.
- [8] C. Lou, Y. Zhang, H. Huang, Q. Wu, H. Chen, S. Liu, Cellformer: Transformer-based nuclei classification with weak supervision for digital pathology, *Medical Image Analysis* 88 (2024) 102859.
- [9] N. Kumar, A. Verma, S. Sharma, R. Bhargava, A. Vahadane, A. Sethi, A dataset and a technique for generalized nuclear segmentation for computational pathology, *IEEE Transactions on Medical Imaging* 36 (2017) 1550–1560.
- [10] J. Huang, H. Li, X. Wan, G. Li, Affine-consistent transformer for multi-class cell nuclei detection, in: *Proceedings of the IEEE/CVF International Conference on Computer Vision (ICCV)*, 2023, pp. 21384–21393.
- [11] F. Hörst, M. Rempe, L. Heine, C. Seibold, J. Keyl, G. Baldini, S. Uğurel, J. Siveke, B. Grünwald, J. Egger, J. Kleesiek, Cellvit: Vision transformers for precise cell segmentation and classification, *Medical Image Analysis* 94 (2024) 103143. URL: <https://www.sciencedirect.com/science/article/pii/S1361841524000689>. doi:<https://doi.org/10.1016/j.media.2024.103143>.
- [12] A. Obeid, T. Mahbub, S. Javed, J. Dias, N. Werghi, Nucdetr: end-to-end transformer for nucleus detection in histopathology images, in: *International Workshop on Computational Mathematics Modeling in Cancer Analysis*, Springer, 2022, pp. 47–57.
- [13] O. Pina, E. Dorca, V. Vilaplana, Cell-DETR: Efficient cell detection and classification in WSIs with transformers, in: *Medical Imaging with Deep Learning*, 2024. URL: <https://openreview.net/forum?id=H4KbJ1AHuq>.
- [14] S. Chen, C. Ding, M. Liu, J. Cheng, D. Tao, Cpp-net: Context-aware polygon proposal network for nucleus segmentation, *IEEE Transactions on Image Processing* 32 (2023) 980–994.

- [15] Z. Cui, J. Yao, L. Zeng, J. Yang, W. Liu, X. Wang, Lkcell: Efficient cell nuclei instance segmentation with large convolution kernels, 2024. URL: <https://arxiv.org/abs/2407.18054>. arXiv:2407.18054.
- [16] U. Schmidt, M. Weigert, C. Broaddus, G. Myers, Cell detection with star-convex polygons, in: Medical Image Computing and Computer Assisted Intervention - MICCAI 2018 - 21st International Conference, Granada, Spain, September 16-20, 2018, Proceedings, Part II, 2018, pp. 265–273. doi:[10.1007/978-3-030-00934-2_30](https://doi.org/10.1007/978-3-030-00934-2_30).
- [17] M. Weigert, U. Schmidt, Nuclei instance segmentation and classification in histopathology images with stardist, in: The IEEE International Symposium on Biomedical Imaging Challenges (ISBIC), 2022. doi:[10.1109/ISBIC56247.2022.9854534](https://doi.org/10.1109/ISBIC56247.2022.9854534).
- [18] N. Carion, F. Massa, G. Synnaeve, N. Usunier, A. Kirillov, S. Zagoruyko, End-to-end object detection with transformers, in: European conference on computer vision, Springer, 2020, pp. 213–229.
- [19] E. Baumann, B. Dislich, J. L. Rumberger, I. D. Nagtegaal, M. R. Martinez, I. Zlobec, Hover-next: A fast nuclei segmentation and classification pipeline for next generation histopathology, in: Medical Imaging with Deep Learning, 2024.
- [20] J. Gamper, N. A. Koohbanani, K. Benes, A. Khuram, N. Rajpoot, Pan-nuke: an open pan-cancer histology dataset for nuclei instance segmentation and classification, in: European Congress on Digital Pathology, Springer, 2019, pp. 11–19.
- [21] K. He, G. Gkioxari, P. Dollár, R. Girshick, Mask r-cnn, in: Proceedings of the IEEE international conference on computer vision, 2017, pp. 2961–2969.
- [22] A. O. Vuola, S. U. Akram, J. Kannala, Mask-rcnn and u-net ensembled for nuclei segmentation, in: 2019 IEEE 16th international symposium on biomedical imaging (ISBI 2019), IEEE, 2019, pp. 208–212.
- [23] O. Ronneberger, P. Fischer, T. Brox, U-net: Convolutional networks for biomedical image segmentation, in: Medical image computing and

computer-assisted intervention–MICCAI 2015: 18th international conference, Munich, Germany, October 5–9, 2015, proceedings, part III 18, Springer, 2015, pp. 234–241.

- [24] B. Bancher, A. Mahbod, I. Ellinger, R. Ecker, G. Dorffner, Improving mask r-cnn for nuclei instance segmentation in hematoxylin & eosin-stained histological images, in: MICCAI workshop on computational pathology, PMLR, 2021, pp. 20–35.
- [25] Y. Song, E.-L. Tan, X. Jiang, J.-Z. Cheng, D. Ni, S. Chen, B. Lei, T. Wang, Accurate cervical cell segmentation from overlapping clumps in pap smear images, *IEEE Transactions on Medical Imaging* 36 (2017) 288–300. doi:[10.1109/TMI.2016.2606380](https://doi.org/10.1109/TMI.2016.2606380).
- [26] P. Naylor, M. Laé, F. Reyal, T. Walter, Segmentation of nuclei in histopathology images by deep regression of the distance map, *IEEE Transactions on Medical Imaging* 38 (2019) 448–459. doi:[10.1109/TMI.2018.2865709](https://doi.org/10.1109/TMI.2018.2865709).
- [27] A. Kirillov, E. Mintun, N. Ravi, H. Mao, C. Rolland, L. Gustafson, T. Xiao, S. Whitehead, A. C. Berg, W.-Y. Lo, P. Dollár, R. Girshick, Segment anything, in: 2023 IEEE/CVF International Conference on Computer Vision (ICCV), 2023, pp. 3992–4003. doi:[10.1109/ICCV51070.2023.00371](https://doi.org/10.1109/ICCV51070.2023.00371).
- [28] X. Ding, Y. Zhang, Y. Ge, S. Zhao, L. Song, X. Yue, Y. Shan, Unireplknet: A universal perception large-kernel convnet for audio video point cloud time-series and image recognition, in: Proceedings of the IEEE/CVF Conference on Computer Vision and Pattern Recognition, 2024, pp. 5513–5524.
- [29] F. Hörst, M. Rempe, H. Becker, L. Heine, J. Keyl, J. Kleesiek, Cel-lvit++: Energy-efficient and adaptive cell segmentation and classification using foundation models, *arXiv preprint arXiv:2501.05269* (2025).
- [30] S. Mandal, V. Uhlmann, Splinedist: Automated cell segmentation with spline curves, in: 2021 IEEE 18th International Symposium on Biomedical Imaging (ISBI), 2021, pp. 1082–1086. doi:[10.1109/ISBI48211.2021.9433928](https://doi.org/10.1109/ISBI48211.2021.9433928).

- [31] D. Hirling, P. Horvath, Fully automatic cell segmentation with fourier descriptors, *bioRxiv* (2021) 2021–12.
- [32] E. Persoon, K.-S. Fu, Shape discrimination using fourier descriptors, *IEEE Transactions on Systems, Man, and Cybernetics* 7 (1977) 170–179. doi:[10.1109/TSMC.1977.4309681](https://doi.org/10.1109/TSMC.1977.4309681).
- [33] O. Vinyals, S. Bengio, M. Kudlur, Order matters: Sequence to sequence for sets, in: Y. Bengio, Y. LeCun (Eds.), *Proceedings of the 4th International Conference on Learning Representations (ICLR)*, San Juan, Puerto Rico, 2016. URL: <https://arxiv.org/abs/1511.06391>.
- [34] A. Vaswani, N. Shazeer, N. Parmar, J. Uszkoreit, L. Jones, A. N. Gomez, L. u. Kaiser, I. Polosukhin, Attention is all you need, in: I. Guyon, U. V. Luxburg, S. Bengio, H. Wallach, R. Fergus, S. Vishwanathan, R. Garnett (Eds.), *Advances in Neural Information Processing Systems*, volume 30, Curran Associates, Inc., 2017.
- [35] T. Prangemeier, C. Reich, H. Koeppl, Attention-based transformers for instance segmentation of cells in microstructures, in: *2020 IEEE International Conference on Bioinformatics and Biomedicine (BIBM)*, 2020, pp. 700–707. doi:[10.1109/BIBM49941.2020.9313305](https://doi.org/10.1109/BIBM49941.2020.9313305).
- [36] Y. Liu, Y. Zhang, Y. Wang, Y. Zhang, J. Tian, Z. Shi, J. Fan, Z. He, Sap-detr: Bridging the gap between salient points and queries-based transformer detector for fast model convergency, in: *Proceedings of the IEEE/CVF Conference on Computer Vision and Pattern Recognition*, 2023, pp. 15539–15547.
- [37] Z. Liu, H. Hu, Y. Lin, Z. Yao, Z. Xie, Y. Wei, J. Ning, Y. Cao, Z. Zhang, L. Dong, F. Wei, B. Guo, Swin transformer v2: Scaling up capacity and resolution, in: *International Conference on Computer Vision and Pattern Recognition (CVPR)*, 2022.
- [38] J. Lammerding, Mechanics of the nucleus, *Comprehensive physiology* 1 (2011) 783.
- [39] C. Schenck, I. Reid, M. G. Jacob, A. Bewley, J. Ainslie, D. Rendleman, D. Jain, M. Sharma, A. Dubey, A. Wahid, et al., Learning the ropes: Better 2d and 3d position encodings with string, *arXiv preprint arXiv:2502.02562* (2025).

- [40] P. Zhang, Y. Chen, R. Su, H. Ding, I. Stoica, Z. Liu, H. Zhang, Fast video generation with sliding tile attention, arXiv preprint arXiv:2502.04507 (2025).
- [41] H. Zhang, F. Li, S. Liu, L. Zhang, H. Su, J. Zhu, L. M. Ni, H.-Y. Shum, Dino: Detr with improved denoising anchor boxes for end-to-end object detection, 2022. [arXiv:2203.03605](https://arxiv.org/abs/2203.03605).
- [42] Anonymous, HoTPP benchmark: Are we good at the long horizon events forecasting?, in: Submitted to The Thirteenth International Conference on Learning Representations, 2024. URL: <https://openreview.net/forum?id=1yJ3IDpb1D>, under review.
- [43] T.-Y. Lin, P. Goyal, R. Girshick, K. He, P. Dollár, Focal loss for dense object detection, IEEE Transactions on Pattern Analysis and Machine Intelligence 42 (2020) 318–327. doi:[10.1109/TPAMI.2018.2858826](https://doi.org/10.1109/TPAMI.2018.2858826).
- [44] A. Kirillov, K. He, R. Girshick, C. Rother, P. Dollár, Panoptic segmentation, in: Proceedings of the IEEE/CVF conference on computer vision and pattern recognition, 2019, pp. 9404–9413.
- [45] K. Sirinukunwattana, S. E. A. Raza, Y.-W. Tsang, D. R. Snead, I. A. Cree, N. M. Rajpoot, Locality sensitive deep learning for detection and classification of nuclei in routine colon cancer histology images, IEEE transactions on medical imaging 35 (2016) 1196–1206.
- [46] J. Gamper, N. A. Koohbanani, S. Graham, M. Jahanifar, S. A. Khurram, A. Azam, K. Hewitt, N. Rajpoot, Pannuke dataset extension, insights and baselines, arXiv preprint arXiv:2003.10778 (2020).
- [47] N. Kumar, R. Verma, D. Anand, Y. Zhou, O. F. Onder, E. Tsougenis, H. Chen, P.-A. Heng, J. Li, Z. Hu, Y. Wang, N. A. Koohbanani, M. Jahanifar, N. Z. Tajeddin, A. Gooya, N. Rajpoot, X. Ren, S. Zhou, Q. Wang, D. Shen, C.-K. Yang, C.-H. Weng, W.-H. Yu, C.-Y. Yeh, S. Yang, S. Xu, P. H. Yeung, P. Sun, A. Mahbod, G. Schaefer, I. Ellinger, R. Ecker, O. Smedby, C. Wang, B. Chidester, T.-V. Ton, M.-T. Tran, J. Ma, M. N. Do, S. Graham, Q. D. Vu, J. T. Kwak, A. Gunda, R. Chunduri, C. Hu, X. Zhou, D. Lotfi, R. Safdari, A. Kasceenas, A. O’Neil, D. Eschweiler, J. Stegmaier, Y. Cui, B. Yin, K. Chen, X. Tian, P. Gruening, E. Barth, E. Arbel, I. Remer, A. Ben-Dor, E. Sirazitdinova, M. Kohl,

S. Braunewell, Y. Li, X. Xie, L. Shen, J. Ma, K. D. Baksi, M. A. Khan, J. Choo, A. Colomer, V. Naranjo, L. Pei, K. M. Iftekharuddin, K. Roy, D. Bhattacharjee, A. Pedraza, M. G. Bueno, S. Devanathan, S. Radhakrishnan, P. Koduganty, Z. Wu, G. Cai, X. Liu, Y. Wang, A. Sethi, A multi-organ nucleus segmentation challenge, *IEEE Transactions on Medical Imaging* 39 (2020) 1380–1391. doi:[10.1109/TMI.2019.2947628](https://doi.org/10.1109/TMI.2019.2947628).

- [48] N. Shazeer, Glu variants improve transformer, arXiv preprint arXiv:2002.05202 (2020).
- [49] I. Loshchilov, F. Hutter, Decoupled weight decay regularization, in: International Conference on Learning Representations, 2019. URL: <https://openreview.net/forum?id=Bkg6RiCqY7>.
- [50] K. He, X. Zhang, S. Ren, J. Sun, Deep residual learning for image recognition, in: Proceedings of the IEEE Conference on Computer Vision and Pattern Recognition (CVPR), IEEE, IEEE Computer Society, Las Vegas, NV, USA, 2016, pp. 770–778. doi:[10.1109/CVPR.2016.90](https://doi.org/10.1109/CVPR.2016.90).
- [51] Okunator, okunator/cellseg_models.pytorch: v0.1.26, 2025. URL: <https://zenodo.org/doi/10.5281/zenodo.15357070>. doi:[10.5281/zenodo.15357070](https://doi.org/10.5281/zenodo.15357070).